Contents lists available at ScienceDirect

Nano-Structures & Nano-Objects

journal homepage: http://ees.elsevier.com

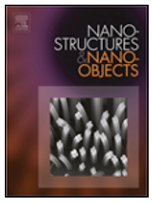

Engineering of colloidal nanocrystal thin films and their optoelectronic properties: A simple and effective route

E.A. Slejko *, L. Cozzarini, V. Lughi

DIA – Department of Engineering and Architecture, University of Trieste, Via Alfonso Valerio 6/1, 34127 Trieste, Italy

ARTICLE INFO

Article history:
Received 7 August 2019
Received in revised form 30 January 2020
Accepted 11 Febraury 2020
Available online xxx

Keywords
Core–shell
Quantum dots
Sintering
Activation energy
Photoluminescence shift
Exciton delocalization

ABSTRACT

This work investigates the effect of heat treatments on CdSe/CdS core–shell nanocrystals assemblies with different sizes and capping ligands. Nanostructured thin films, consisting of an array of CdSe quantum dots embedded in a continuous matrix of CdS, have been obtained by mild thermal treatments of CdSe/CdS core–shell nanocrystals deposited on glass substrates from colloidal solution. These materials are regarded as promising photon upconverters, or absorbers for high-efficiency photovoltaic devices. The treatments were conducted in the range 300–550 °C for up to 150 min. The nanoscale evolution during the heat treatment was investigated by monitoring optical properties of the films. Initially, the well-defined photoluminescence band, corresponding to the first quantum dots exciton state, rapidly shifts towards lower energy, indicating delocalization of the exciton and suggesting that nanocrystal CdS shells are merging by sintering mechanisms, thus forming a continuous matrix. Control over this phase of the heat treatment leads to the desired nanoscale morphology and properties. The kinetics of sintering has been characterized, and the procedure has been systemically applied to CdSe/CdS nanocrystals of different sizes and ligand types. This research provides novel values for the activation energy of the sintering process and strongly support the general applicability of such process to control and optimize optoelectronic properties of nanostructured thin films for applications like light-emitting diodes, tunable emitters and photoconductors among others.

1. Introduction

In recent years, remarkable improvements have been achieved in the nanotechnology field about the synthesis [1–3], composition control [4,5], shape determination [6] and surface chemistry [7,8] of nanocrystals (NCs). While lots of applications rely on NCs in colloidal form, like for example drug delivery, catalysis and biological labeling [9–11], many others require the assembly and deposition of these building blocks to obtain three-dimensional structures [12,13]. Even if the physics and chemistry behind deposition techniques may seem simpler compared to colloids processing, it is a fundamental procedure to fabricate devices with specific properties for medical, optical and electronic applications. Being able to organize and control the disposition of NCs in three-dimensional solids, without sacrificing their properties or even better by exploiting possible emerging properties arising from the synergy between the elements of the nanosystem, is therefore an extremely important operation. Such structures can find application in several fields, like for example as solution-processable thermoelectric materials due to the importance of grain boundaries to attain low thermal conductivity, or as solution-based materials for low-cost and large-area solid state electronics [13–15] among many others. Being able to propose simple and effective processes to control the size, shape, ordered arrangement and functional properties of NCs is a much-needed feature of current state-of-the-art to help the community in designing and producing innovative devices. For example, semiconductor nanocrystals have been proposed as viable candidates to obtain an intermediate band material [16–18]. In a three dimensional, ordered array of QDs located inside another, larger bandgap semiconductor material (referred as *barrier* or *host* material), an IB would arise within the bandgap of the host material from the confined electronic states of the QDs if the electron wave functions become delocalized and have significant overlap [19]. This geometry, also known as *Quantum Dots Supracrystal* [20,21], has been obtained in other works by molecular beam epitaxy, and working IB solar cells with this structure have been reported [22,23].

This work proposes an alternative, bottom-up approach to obtain such complex geometry starting from colloidal synthesis of core–shell nanocrystals. These nanocrystals have been self-assembled and then densified after the application of a mild heat treatment conceived to sinter the external shell material, becoming the "host" matrix while preserving the inner quantum dots. CdSe/CdS core–shell NCs were synthesized by colloidal routes similar to those reported by other authors [24,25] as they represent the prototypical system for core–shell

* Correspondence to: DIA – Department of Engineering and Architecture, University of Trieste, Via Valerio 6/1, 34127 Trieste, Italy.
E-mail address: easlejko@units.it (E.A. Slejko)

https://doi.org/10.1016/j.nanoso.2020.100432
2352-507/

II–VI semiconductor quantum dots. Most synthetic routes to high quality NCs with tunable sizes and shapes utilize long hydrocarbon molecules containing a coordinating head-group as ligands (typically carboxylic acids, amines and phosphines), which sterically stabilize nanocrystals in non-polar solvents [7,13,26,27]. The presence of these long, insulating molecules creates a barrier around each NC and blocks the access of other species to the nanocrystal surface; nevertheless, these organic ligands remain bonded on NCs surface even during the annealing step, and can represent a physical barrier, as well as an electric one, to the external shell material sintering process [28]. A previous study [29] shows that long chain carboxylic acids remain bound on NC surfaces up to temperatures higher than 400 °C, well above their boiling points. Therefore, they are not easily removed by applying a heat treatment, at least not without exposing the heterophasic core–shell nanocrystal to an unwanted alloying process [30]. In this work, it was preferred to chemically substitute them with short chain thiols (like mercaptoacetic acid), to ease their subsequent removal by means of heat treatment, or by replacement with short functional ligands like S^{2-}, by means of colloidal Atomic Layer Deposition (c-ALD), which can be incorporated on the surface of the shell due the chemical likeliness to shell material [14,31]. The selected ligands have low boiling point (between 100 and 220 °C), and are known to be desorbed from the surface of CdS nanocrystals between 190 and 250 °C [32]. The final heat treatment application was therefore conceived to sinter the external shell material while preserving the nanostructure, i.e. avoiding the alloying of core and shell materials. Sintering can be seen as a densification method based on atomic diffusion [33]; being a thermally activated process, diffusion occurs much faster at higher temperatures. In most sintering processes, the material is heated to a sintering temperature T_s below the melting point T_m; typical values for sintering are $T_s \approx 2/3\ T_m$. The atoms diffuse across the boundaries of crystallites, fusing the particles together and therefore creating bigger crystallites. The driving force for this process is the change in free energy E, which has two contributes: (i) the decrease in surface area and (ii) the reduction of the surface free energy by the replacement of solid–vapor interfaces with solid–solid interfaces. If the size of the particle is small, or, equivalently, if the radius of curvature is large, these effects become very large in magnitude, leading to sintering and even melting at lower temperatures. It is also known that melting temperature of nano-sized crystals decreases with dimension; Goldstein and co-workers [32] reported a difference between bulk CdS melting temperature and nano-sized CdS melting temperature larger than 1000 K for crystallite with a radius below 2 nm. According to their work, CdS crystallites with a diameter ranging between 6–7 nm (about the size of nano-heterostructures used in this work) should have a melting temperature $T_M \approx 825$ °C; therefore, a good sintering temperature for these crystallites is ≈ 550 °C. The optimal sintering temperature and time were determined experimentally, following the bandgap evolution of CdS NCs and CdSe/CdS core–shell NCs during the heat treatments via fluorescence spectroscopy. Our approach relies on simple processing and low-cost fabrication of thin films with precise optoelectronic properties. In fact, the majority of processes proposed so far requires vacuum and/or multi steps processing to limit formation of defects and impurities. Stabilizing NCs with short ligands allowed us to reduce the temperature during annealing, avoiding the drawbacks encountered in literature [29,34–36].

The aim of this work was the investigation of how sintering affects the optoelectronic properties of semiconductor NCs thin films made of CdSe/CdS and the fine tuning of such properties by means of control of temperature and sintering time. In this work we have performed the synthesis of core–shell nanocrystals in organic media, followed by ligand exchange. We investigated two different systems of CdSe/CdS core–shell: one stabilized with mercaptoacetic acid (MAA) and one with Sulfur ions (S^{2-}), see Fig. 1. Heat treatments have been performed on the films and their emission has been characterized at different time and temperature of the process.

2. Material and methods

Materials. All chemicals have been used as received, without further purification. Cadmium oxide (CdO, 99.5%), oleic acid (90%), trioctylphosphine (TOP, 90%), 1-octadecene (ODE, 90%), selenium powder (99.999%), sulfur powder (99.98%), cadmium acetate dihydrate ($Cd(OAc)_2 \cdot 2H_2O$, 99.99%), *n*-methylformamide (MFA, 99%), sodium sulfide (Na_2S, 97%), methanol (>99.8%), ethanol (>99.5%), acetone (>99,9%), n-hexane (>95%), mercaptoacetic acid (MAA, > 98%), cadmium sulfide powder (CdS, > 99%), cadmium selenide powder (CdSe, >99%) were purchased from Sigma-Aldrich.

Synthesis of CdS NCs. Sulfur powder (22 mg) was dissolved in 0.5 ml TOP and 1.5 ml ODE, at room temperature. In a three-neck flask under argon flow, 135 mg of cadmium acetate, 10 ml ODE and 0.4 ml OA were heated at 260 °C for 10 min, then the previously prepared Sulfur solution was quickly injected, . The temperature was kept at 250 °C for 45 min in order to grow CdS NCs with first absorption peak centered at 466 nm (corresponding to a diameter of 5 nm). Size and concentration were determined according to Yu et al. [38] sizing curves. After synthesis, particles were stored at room temperature in their original growth solution.

Synthesis of CdSe NCs. Selenium powder (80 mg) was dissolved in TOP and ODE (0.5 ml and 1.5 ml respectively) at room temperature.

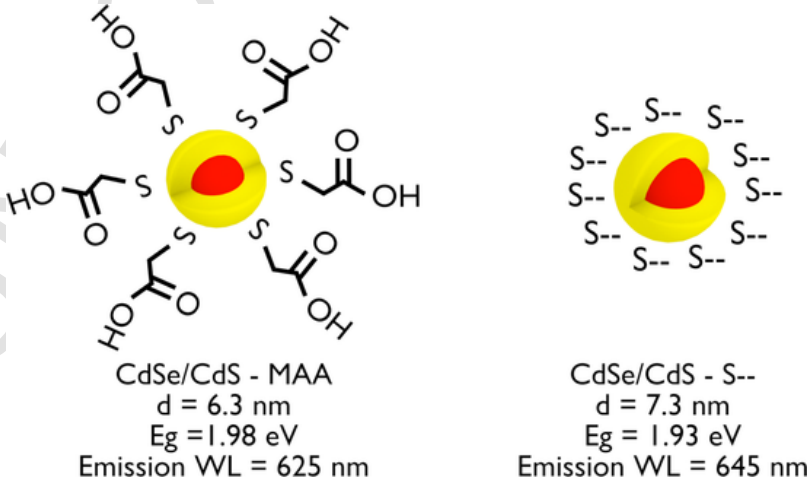

Fig. 1. Conceptual representation of the two experimental systems developed in this contribution and their optoelectronic characteristics. The red core represents the CdSe, while the yellow shell indicates CdS. In detail: CdSe/CdS core–shell stabilized with mercaptoacetic acid (left) and CdSe/CdS core–shell capped by S^{2-} (right) with respective mean size, bandgap and emission wavelength.

In a three-neck flask, 135 mg of cadmium acetate, 10 ml ODE and 0.4 ml OA were heated at 280 °C under argon flow for 10 min, then the previously prepared Selenium precursor was quickly injected. The temperature was kept at 250 °C for 15 min in order to grow CdSe NCs with first absorption peak centered at 565 nm (corresponding to a diameter of 3.5 nm)[37]. Size and concentration were determined according to Janiesak et al. [39] sizing curves. Before shell growth, particles were washed twice in methanol/acetone to remove reaction byproducts, centrifuged, re-dissolved and finally stored in ODE for shell growth.

Synthesis of CdSe/CdS core–shell NCs. A preselected amount of CdSe NCs of known size and concentration was diluted in 15 ml ODE into a three-neck flask and heated to 240 °C under argon flow; then, pre-calculated amounts of cadmium and sulfur precursor solutions were alternatively injected into the reaction vessel. A slightly modified Selective Ion Layer Adsorption and Reaction (SILAR) method was used [25]. Sulfur precursor was prepared by dissolving 6.4 mg of S in 0.1 ml TOP and 4 ml ODE at room temperature; cadmium precursor was prepared by heating 324 mg of cadmium acetate in 4.2 ml ODE and 1.8 ml of OA at 250 °C for 20 min in inert atmosphere. Reaction temperature was kept between 240 °C and 250 °C; reaction time for each ML from 5 to 10 min. Up to 5 MLs of CdS were grown on CdSe cores. After the reaction was complete, the mixture was cooled to room temperature. After the deposition, the samples have been washed with methanol and acetone, precipitated and dispersed in fresh hexane. Size was estimated through a Concentric Spherical Model (reported by van Embden et al. [24]). Control over size and size distribution during core synthesis and shell deposition is reported in Figure S1.

2.1. MAA System

Ligands exchange procedure. 0.1 mmol of CdSe/CdS core–shell NCs or 0.1 mmol of CdS NCs were washed twice with methanol, precipitated with acetone and re-dissolved in 4 ml of n-hexane; 0.1 mmol of MAA were added; the NCs started aggregation/flocculation almost immediately; the suspension was vigorously stirred for 30–60 min, then it was divided in two test tubes; 2 ml of n-hexane and 2 ml of acetone were added to each tube, vigorously mixed, then centrifuged for 10 min. At this point, a colored precipitate appeared in the bottom of the test tubes: the precipitate was then washed and centrifuged/precipitated twice with n-hexane, then it was dispersed in 2 ml ethanol.

Deposition of colloidal solution. Glass microscope slides (Corning, 75 × 25 mm, plain, purchased from Sigma-Aldrich) were cleaned by two-step sonication: 5 min ultrasonic cleaning in acetone, dried with nitrogen flow, then 5 min ultrasonic cleaning in 2-propanol, finally dried with nitrogen flow; a Branson 2200 Ultrasonic Cleaner was used. Samples were then cut into 5 mm x 5 mm pieces and heated to 50 °C on a hot plate. MAA Ligand-exchanged NCs were drop casted on hot glass substrates from ethanol dispersion (2 drops for a 5 × 5 mm^2 glass substrate); after solvent evaporation, samples were removed from the hot plate and inserted inside glass tubes. Before sealing the tubes, nitrogen has been flowed inside to remove oxygen and avoid oxidation during the following thermal treatment.

Heat treatments. Heat treatments were performed in a Linn High Therm VMK 1800 furnace; NCs assembled on 5 × 5 mm glass substrates inside sealed tubes were put on aluminum oxide holders and heated to 300 °C, 350 °C, 400 °C and 500 °C, for a maximum duration of 150 min. Temperature higher that 600 °C would soften the tube glass walls, causing potential leakage of inert gas.

2.2. S^{2-} system

Ligands removal and phase transfer procedure. Aliquots of core–shell NCs in hexane have been mixed with large excess of sodium sulfide (1000x times the amount of surface sites) in N-methylformamide. The transfer from non-polar to polar media happened within few seconds [31]. Crystals have been, then, centrifuged and precipitated using hexane and acetone, and finally redispersed in fresh MFA.

Deposition of colloidal solution. The stable NCs solution was deposited on glass substrate by drop-casting in order to obtain thin films. N-methylformamide is a high boiling point solvent, and its complete spontaneous evaporation could require long time. To address this limitation, substrates with drop-casted solution have been placed inside a vacuum chamber in order to promote fast controlled evaporation. No heating has been applied to avoid any possible event of annealing or sintering, which would reduce sensibly the repeatability of the process. Glass microscope slides have been sonicated 5 min in acetone and 5 min in isopropanol. Slides have been cut in small rectangular substrates with size 5 × 5 mm^2. Two drops of 4.9 μM NCs in MFA solution have been deposited on the substrates, then samples have been placed inside the vacuum chamber connected with a water pump. Evaporation occurred during the following two days. Once films were completely dried, they have been inserted inside glass tubes. Before sealing, nitrogen flux flowed inside the tubes to remove oxygen and avoid oxidation during the following thermal treatment.

Heat treatment. Samples inserted in glass tubes with controlled nitrogen atmosphere have been sintered at various temperatures, from 300 °C up to 550 °C. Every series presented 7 different samples, each one with a different treatment duration: 2, 4, 8, 16, 32, 64 and 128 min. After the treatment, samples inside the tubes have been cooled down in air, the glass was broken and films have been optically characterized. Fig. 2 indicates the synthetic procedures from the core synthesis to the final thermal treatment for the two systems.

2.3. Characterization

TEM imaging. Diluted solution of NCs in n-hexane were obtained washing original solutions twice in methanol, precipitating with acetone, then re-dissolving in n-hexane. Samples were prepared by drop-casting these diluted solutions on TEM grids (Electron Microscopy Science CF-200 carbon/copper); images were acquired using a Philips EM208 Transmission Electron Microscope. NCs size were directly measured on TEM images, using ImageJ software.

IR spectra of surface ligands. Original ligands: NC samples were taken directly from synthesis solution, washed twice with methanol, precipitated with acetone and re-dissolved in n-hexane, then drop-casted on a IR-transparent ZnSe window. Ligands-exchanged samples were drop-casted on a ZnSe window from methanol or ethanol dispersions. After solvent evaporation, the IR-transparent window was placed into a sample holder inside the experimental chamber of a Thermo Nicolet Nexus 470 FT-IR spectrometer (operated through a Nicolet In-

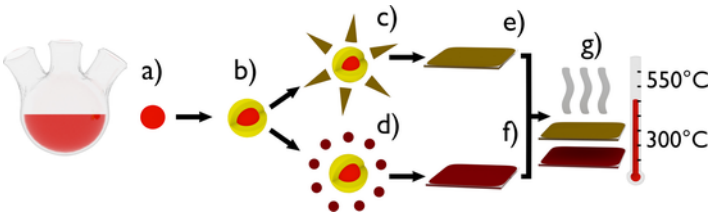

Fig. 2. Conceptual scheme of the synthetic processes in this contribution. (a) synthesis of core CdSe; (b) CdSe/CdS core–shell development; (c) and (d) ligands exchange with MAA and S^{2-}, respectively; (e) and (f) deposition of the colloidal solution on glass films; (g) thermal treatment of samples.

truments Omnic 5.2 software); IR spectra were acquired between 4000 and 500 cm^{-1} at a resolution of 0.48 cm^{-1}.

Optical characterization of colloidal solutions. Absorption and photoluminescence (PL) spectra were acquired at regular intervals during synthesis of NCs. Small aliquots were extracted from reaction solution, diluted in 2 ml n-hexane and placed in a cuvette (Plastibrand® standard disposable PMMA cuvette, path length 10 mm). A Perkin-Elmer Lambda Bio 20 spectrophotometer was used to record UV–VIS absorption spectra, in wavelength range between 300 and 800 nm, with a resolution of 0.5 nm. Photoluminescence spectra were acquired through an OceanOptics SD2000 spectrophotometer, in wavelength range between 250 and 850 nm, with a resolution of 0.36 nm, using an excitation source of 320 nm. First exciton wavelength λ, corresponding to the lowest energy absorption peak, was determined taking the minimum of the second derivative of the absorption spectrum, applying the Savitzky–Golay method in ThermoGalactic Grams/AI 7.02. Emission wavelength was determined from peak position of photoluminescence spectrum, fitted with Gaussian or log-normal curves, using ThermoGalactic Grams/AI 7.02.

Photoluminescence measurements of deposited films. PL spectra of as-deposited samples, of heat-treated samples and of commercial available CdS and CdSe powders were acquired through a Renishaw In-Via Raman Microscope equipped with a RenCam CCD detector, operated by a Renishaw Wire 3 software [40]. Peak positions were determined by fitting spectra with log-normal curves using ThermoGalactic Grams/AI 7.02. Excitation sources were an Omicron Bluephoton® 480 mW diode laser emitting at 405 nm (used for CdS NCs and CdS films during heat treatment), a SpectraPhysics 50 mW argon-ion laser emitting at 514.5 nm and a Renishaw HP NIR 300 mW diode laser emitting at 785 nm (used for CdSe/CdS NCs and film during heat treatment).

3. Result and discussion

CdSe NCs were synthesized from cadmium acetate, oleic acid, selenium and trioctylphosphine with a modified method (see experimental details) based on previously reported techniques [41]; then, 5 monolayers (ML) CdS shell were overgrown to obtain CdSe/CdS core–shell nanocrystals with a successive ion absorption and reaction (SILAR) method similar to that reported by other authors [24,25]. We used cadmium acetate, oleic acid, sulfur and trioctylphosphine as reagents. Fig. 3 left reports absorbance spectra of CdS (synthesized as a reference) and CdSe NCs used in the following steps. TEM pictures of CdSe NCs before shell growth (d = 3.5 ± 0.5 nm, λ_{emi} = 580 nm, first exciton energy = 2.14 eV), reference CdS and CdSe/CdS (5 CdS shell layers - d = 6.3 ± 0.5 nm, λ_{emi} = 625 nm, first exciton energy = 1.98 eV) are shown in Fig. 3 right.

CdSe/CdS long chain ligands were substituted with shorter mercaptoacetic acid (MAA) or S^{2-}, to ease their subsequent removal during heat treatment (see experimental section for details of these procedures), then dispersed in ethanol (in case of MAA) or N-methylformamide (for S^{2-}). For MAA, ligand exchange was assessed by means of infra-red spectroscopy (see Figure S2), while for S^{2-} the transfer from nonpolar to polar solution, supported by PL spectra, was considered as indication of the ligand exchange (Figure S3).

3.1. MAA-system

Core–shell assemblies were subjected to heat treatments, while monitoring their PL evolution during annealing at 300 °C, 350 °C, 400 °C and 500 °C. Fig. 4 summarizes their PL energy evolution as a function of heating time for each temperature series. It is possible to notice that during heat treatment the PL energy of CdSe/CdS core–shells initially decreases, accordingly to literature [42], from the original value of 1.98 eV down to a common value of 1.84 eV, then it increases to energies even higher than the original NC apparent bandgap. It can be observed that both variations are faster at higher temperatures, as indicated in Fig. 4-right where linear fitting lines represent the transformation rates in the first minutes of the sintering event. Both processes behave like thermal activated ones, and, from the transformation rates, activation energies can be estimated for sintering of external material and reciprocal diffusion of CdSe into CdS, i.e. alloying, resulting in 68 kJ/mol and 126 kJ/mol respectively. These values are in accordance to what previously reported in literature for NCs cation exchange and diffusion mechanisms [43,44].

These films have been compared to reference CdS films synthesized following the same procedure: Fig. 5 shows the first exciton energy as a function of heating times at different temperatures for bare CdS film . It is possible to see that the PL energy of CdS NCs decreases with heat treatment time, analogously to CdSe/CdS films; from original value of 2.7 eV down to a value that is comparable to the bandgap E_G of commercial-available CdS powder. The value of 2.3 eV, lower than the reference bulk material (2.42 eV) is very likely due to defects present in the barrier material, which do act as donor–acceptor pairs, slightly decreasing the apparent bandgap of the material [45–47].

In spherical NCs the relation between radius r and nanocrystal bandgap E_{NC} can be expressed using the formula from Brus et al. [48], where E_G^{bulk} is the bandgap of the bulk material, m_e* and m_h* are electron and hole effective masses, h the Planck's constant, e the elementary charge and ϵ the absolute permittivity of bulk material:

$$E_{NC} = E_G^{bulk} + \frac{h^2}{2r^2}\cdot\left(\frac{1}{m_e^*}+\frac{1}{m_h^*}\right) - \frac{1}{r}\cdot\frac{1.8e^2}{\epsilon}$$

A first exciton energy decrease is consistent with an increase in crystallite dimension, i.e. NCs merging together, since both electron confining potential E_E and hole confining potential E_H decrease [49,50]. When crystallites become larger than Bohr radius, E_{NC}

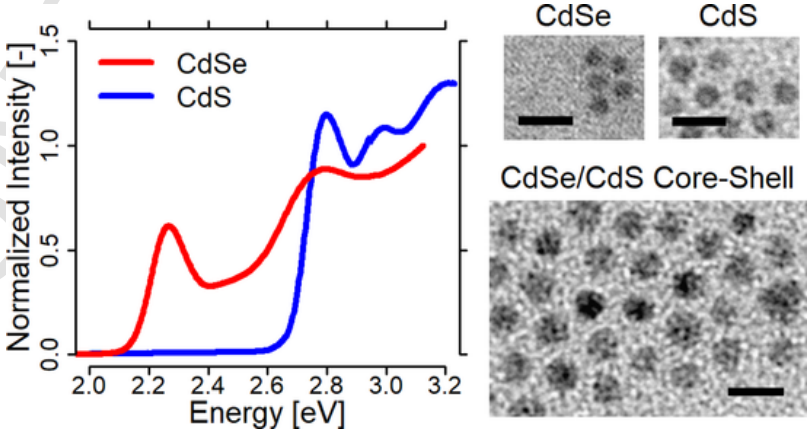

Fig. 3. Absorbance spectra for CdS and CdSe cores (left). TEM image of CdSe core, CdS core and CdSe/CdS core–shell NCs; scale bars are 10 nm (right).

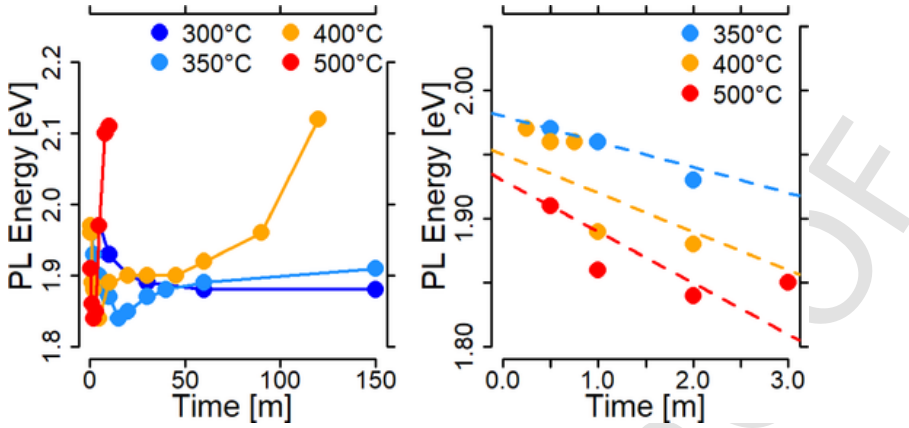

Fig. 4. Left: bandgap energy of CdSe/CdS core–shell NCs capped with MAA as a function of heat treatment time for different temperatures: 300 °C, 350 °C, 400 °C and 500 °C. Right: detail of the first 3-minute region and estimation of the transformation kinetic rate of the system for each temperature series.

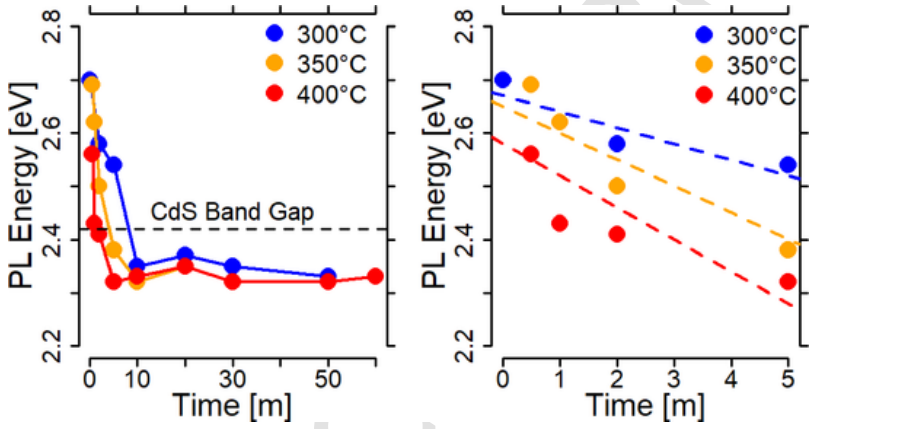

Fig. 5. Left: first exciton energy of CdS NCs as a function of heat treatment time for 300 °C, 350 °C and 400 °C. Dashed line represents the bandgap of commercial CdS powder. Right: linear interpolations of first experimental points to obtain kinetic rate for each temperature series.

approaches the value of the bulk material E_G (as schematized for CdS in Fig. 6).

In the case of CdSe/CdS the situation is slightly different. The bottom energy bandgap threshold is higher than the bandgap of commercial-available CdSe powder, 1.84 eV and 1.74 eV, respectively, leading to the likely conclusion that CdSe cores are not merging together. Given the particular band offset of CdSe/CdS heterojunction, represented in Fig. 7 left, and being E_{NC} the sum of (i) bulk material bandgap E_G; (ii) electron confining potential E_E and (iii) hole confining potential E_H, this implies that after merging the external material (CdS) only E_E should decrease, while E_H should not (holes remain confined into CdSe quantum wells — as schematized in Fig. 7 right). The initial bandgap energy decrease is therefore consistent with an increase in shell dimension only: the external material is merging together and electrons in conduction band are more delocalized. Varying shell thickness of the starting material would affect the interparticle distance between cores within the deposited film, thus allowing the fine-tuning of the optoelectronic properties of the final material.

On the contrary, the successive bandgap energy increase is consistent with alloying of CdSe and CdS: the bandgap of the alloyed material changes as a function of composition, according to Vegard's Law.

$$E_G^{CdSe_xS_{(1-x)}} = xE_G^{CdSe} + (1-x)E_G^{CdS} - b(1-x)$$

where E_G^{CdSe} and E_G^{CdS} are the bandgaps of bulk CdSe and CdS, respectively, and b a deviation from linear behavior, known as "bowing parameter" , which depends on the difference in electronegativity of

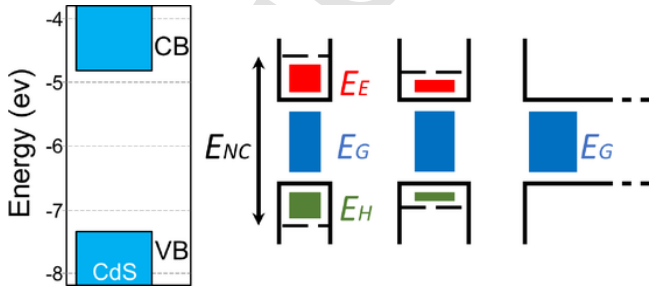

Fig. 6. Schematization of apparent bandgap decrement with increasing CdS NCs size: apparent bandgap E^{NC} is represented by the sum of bulk material bandgap E^G (blue bar), electron confining potential E^E(red bar) and hole confining potential E^H(green bar).

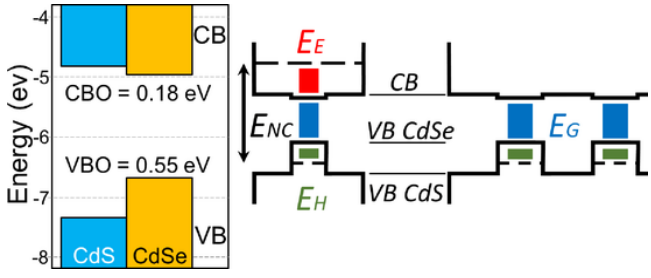

Fig. 7. Left: bulk band offset in a CdSe/CdS heterojunction. Right: schematization of the apparent bandgap, decreasing while the CdS shell is merging together, in CdSe/CdS core–shell NCs. Apparent bandgap E^{NC} is represented by the sum of bulk CdSe bandgap E^G (blue bar), electron confining potential E^E(red bar, decreasing while CdS shell merge together) and hole confining potential E^H(green bar, not influenced by CdS shell merging).

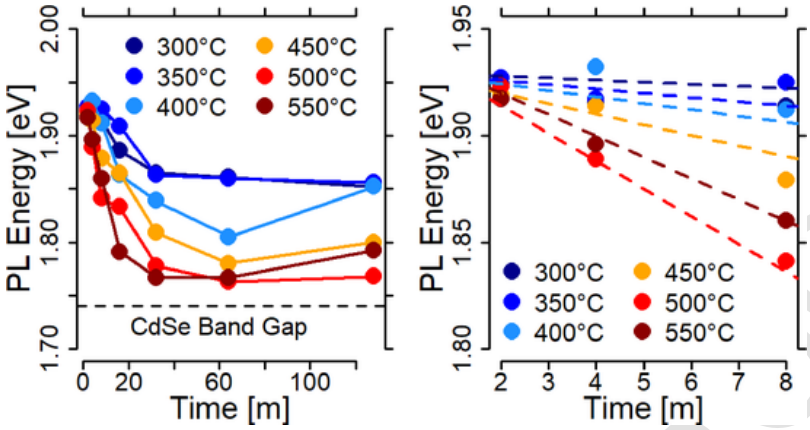

Fig. 8. Left: first exciton evolution during sintering at different temperatures (from 300 °C up to 550 °C), as a function of sintering time, for CdSe/CdS core–shell NCs capped with S^{2-}. Right: first minutes of the transformation and linear fitting (dashed lines) for the evaluation of kinetic rates of the same system.

the two components. Core–shell NCs used in this study were composed by a CdSe core with a diameter of 3.5 nm, and a 5ML-thick CdS shell, corresponding to a molar ratio *S/Se* of 2.44 (that is a $CdSe_x\ S_{(1-x)}$ alloy with $x = 0.3$). Under this assumptions, this compound should have a bulk material E_G of about 2.15 eV, very close to the final two measurements for the 500 °C treatment.

3.2. S^{2-}-system

After shell growth by SILAR, hydrocarbon long-chain molecules are bounded on NCs surface, which stabilize them in organic media. This capping layer would represent an obstacle for the successive self-assembly of nanocrystals, especially in terms of functional properties. Organic compound shells hinder the electron transfer from one NCs toward the neighbors, suppressing any conductive properties the structure may possess. The most promising system consists on the ligand-exchange by means of sodium sulfide. It is worth mentioning that, even by changing long-chain organic compounds with conductive or extremely short ligands, during the self-assembly process these molecules would remain attached on the surface of NCs, representing in most cases impurities for the assembled film and preferential centers of non-radiative recombination. Pyrolysis of these compounds would produce new defects with unspecified composition, increasing the degree of uncertainty related to the structure. These considerations are the main reason for the endeavours to stabilize NCs in polar media using ligands that can be embedded within the shell structure [51,52]. In fact, sulfur ions on the crystal surface represent one additional half monolayer of CdS shell, maintaining compositional coherency, and the sodium counterions in solution can act as p-type dopants of the barrier material once the shell has been sintered. Fig. 8 presents an overview on the evolution of the emission wavelength. As one can observe, there is a substantial PL redshift during the treatment. The redshift is, furthermore, more pronounced at higher temperature, supporting one more time the thermal activation feature of the sintering process. Redshift of photoluminescence is a forecasted effect during sintering, since the electrons within the core–shell perceive an increased delocalization of their wave function, i.e. a weakening of quantum confinement, due to rearrangement of CdS shell material. It is worth noting that PL shift from the starting 1.93 eV toward smaller values , depending on process temperature and time. Small shifts are associated to lower temperature, as for 300 °C and 350 °C the minimum energy reached is 1.86 eV, while at 500 °C the structure presents an emission peak located at 700 nm (1.77 eV). The Arrhenius plot for this transition indicates an activation energy of 63 kJ/mol, slightly lower compared to the one of the system capped with MAA (68 kJ/mol) but not significantly different (Fig. 9). In fact, these figures indicate the amount of thermodynamic energy required during the sintering process, irrespective of the rates of such transformation. As in all systems we are observing sintering of CdS, we do expect, indeed, values quite close to each other.

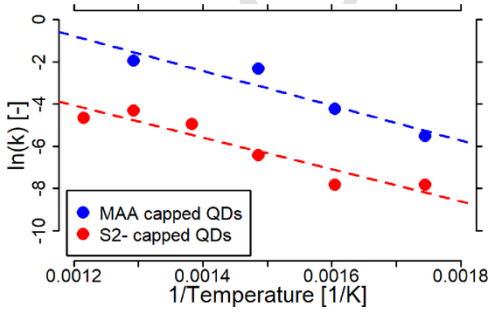

Fig. 9. Arrhenius plot for bandgap energy variation (blue: crystal with MAA red: crystal with S^{2-}) in CdSe/CdS NCs. Dashed lines represent linear fitting of the experimental data. The slope of these lines is associated to the activation energy of the process, in this case 68 and 63 kJ/mol for MAA-capped and S^{2-}-capped NCs, respectively.

The PL emission of sintered films obtained from CdSe/CdS stabilized with S^{2-} is extremely close to the 1.74 eV figure of commercial CdSe, following the same transformation already discussed for MAA-stabilized NCs (Fig. 6). One possible speculative explanation for the difference in film emission wavelengths for the two systems is that NCs stabilized with MAA did not reach a bandgap close to the bulk value because the set in of alloying processes. In fact, as can be seen from Fig. 4, the three higher temperature series abruptly change trend, while for lower temperature there is no evidence of a stable equilibrium in emission wavelength during the time-window we investigated. On the other hand, for S^{2-}-capped NCs a blueshift of film emission wavelength has not been detected, and the system was in the condition to reach equilibrium with a bandgap value close to the one of the massive material. Further investigation is on progress to understand why the two systems have showed a different behavior in the intermediate and final stages of the thermal treatment.

3.3. Homogeneity of the films

To investigate the uniformity in PL emission of samples, we performed an extended analysis on films stabilized with S^{2-} ligands. Samples have been excited by a 514 nm laser source on an area of 400x 650 μm^2 centered in the middle of the film, collecting photoluminescence from an average of 80 spots per sample within that area (see scheme in Fig. 10a). The map colors in Fig. 10c are associated to the detected emission wavelength and provides a general view about the uniformity of the film in terms of photoluminescence . Furthermore, a degradation of the film uniformity occurs during the process, and it is easily noticed by observing the color distribution in each single

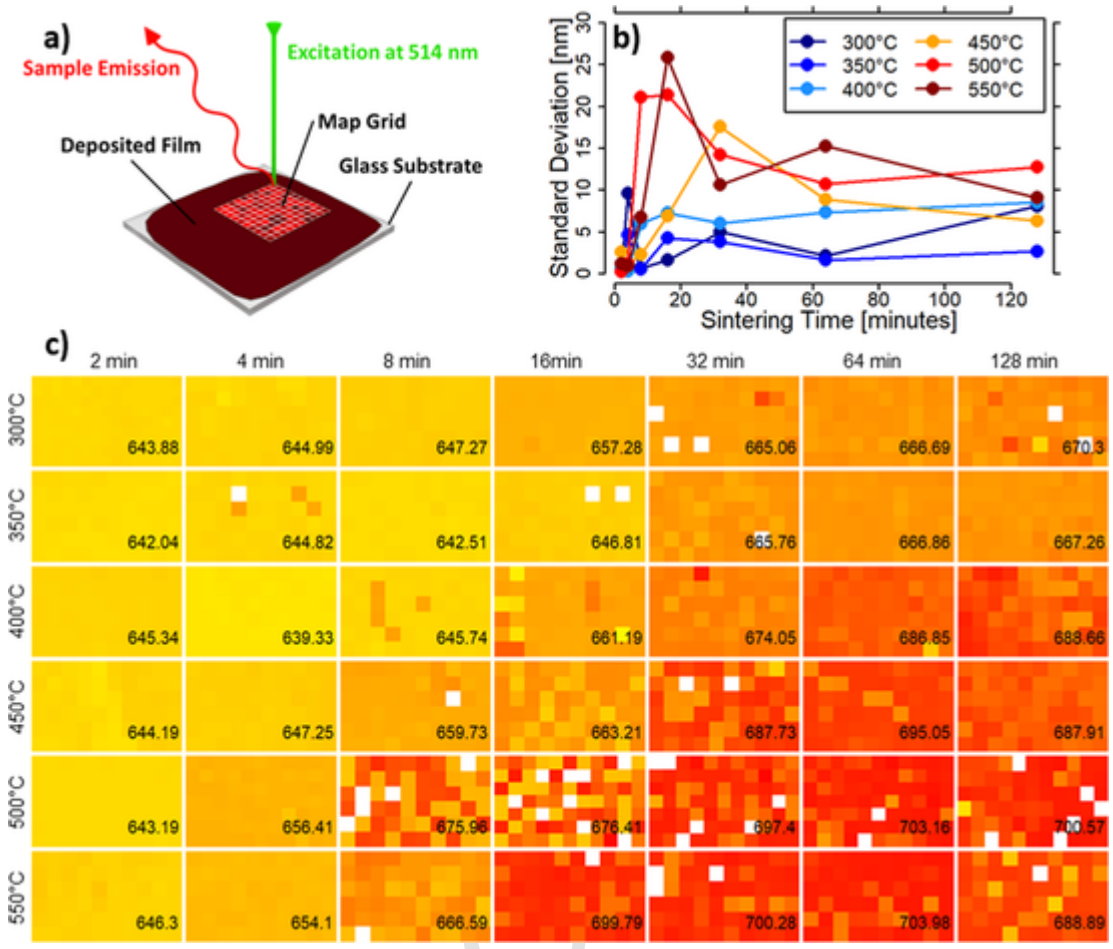

Fig. 10. (a) scheme of the experimental setup for film uniformity analysis under an excitation source at 514 nm. (b) evolution of standard distribution with sintering time for different temperatures of CdSe/CdS core–shell NCs capped with S^{2-} films. Values of standard deviation are obtained from map analysis; a clear trend is observable, with higher temperature processes showing larger standard deviation of emission wavelength. (c) emission maps showing evolution of PL wavelength during sintering of CdSe/CdS core–shell NCs capped with S^{2-}. On the bottom right corner of each map, mean emission wavelengths are reported. White squares inside the maps indicate spots where the peak was not detectable.

map. Higher temperatures cause a degradation of film uniformity, as they promote faster kinetics of transformation and thus result in a less uniform film, Fig. 10b. Low temperatures, on the other side, promote a slow and uniform sintering process on films. It is very unlikely this degradation is caused by oxidation of films, a usually detrimental event, as samples have been sealed inside nitrogen-filled tubes. This reasoning is furthermore supported by the complete absence of substantial blueshift in the first stages of the thermal treatment, an unavoidable occurrence during oxidation [53,54]. Instead, the distribution of PL is due to coalescence and crystal growth, a direct result of heating in inert atmosphere.

4. Conclusion

We have introduced a simple and effective technique for the deposition of multiphase thin films made of II–VI semiconductor nanocrystals and stabilized with different short ligand types. The photoluminescence evolution of these complex structures at high temperatures has been studied, indicating how spectroscopic methods are effective ways to monitor the sintering process of core–shell nanocrystals. All films showed a redshift of their photoluminescence during the process, in accordance to delocalization of the electron wave function in CdSe/CdS core–shell due to conduction band alignment. Furthermore, our results suggest that the process parameters can be easily controlled to obtain films with desired properties. Finally, estimations of the activation energy for the transformation have been determined, resulting in an activation energy of 68 and 63 kJ/mol for MAA- and S^{2-}capped NCs, respectively. Such values provide useful insight in identifying the limiting mechanism and offer further understanding on the physical and chemical processes governing atomic diffusion at the nanoscale. These results are consistent with a model based on the sintering of CdS shell material, while preserving the integrity of CdSe cores, and the development of functional heterostructures with desired properties for electronic and optoelectronic applications.

CRediT authorship contribution statement

E.A. Slejko: Methodology, Validation, Investigation, Data curation, Writing - original draft, Writing - review & editing, Visualization. **L. Cozzarini:** Methodology, Validation, Investigation, Writing - original draft. **V. Lughi:** Conceptualization, Resources, Supervision, Project administration.

Declaration of Competing Interest

The authors declare that they have no known competing financial interests or personal relationships that could have appeared to influence the work reported in this paper.

Formatting of funding sources

This research did not receive any specific grant from funding agencies in the public, commercial, or not-for-profit sectors.

Appendix A. Supplementary data

Supplementary material related to this article can be found online at https://doi.org/10.1016/j.nanoso.2020.100432.

References

[1] N.T.K. Thanh, N. Maclean, S. Mahiddine, Mechanisms of nucleation and growth of nanoparticles in solution, Chem. Rev. 114 (2014) 7610–7630, doi:10.1021/cr400544s.

[2] S.G. Kwon, T. Hyeon, Formation mechanisms of uniform nanocrystals via hot-injection and heat-up methods, Small 7 (2011) 2685–2702, doi:10.1002/smll.201002022.

[3] M. Alizadeh-Ghodsi, M. Pourhassan-Moghaddam, A. Zavari-Nematabad, B. Walker, N. Annabi, A. Akbarzadeh, State-of-the-art and trends in synthesis, properties, and application of quantum dots-based nanomaterials, Part. Part. Syst. Charact. 36 (2019) 1–20, doi:10.1002/ppsc.201800302.

[4] A. Albanese, P.S. Tang, W.C.W. Chan, The effect of nanoparticle size, shape, and surface chemistry on biological systems, Annu. Rev. Biomed. Eng. 14 (2012) 1–16, doi:10.1146/annurev-bioeng-071811-150124.

[5] C. de M. Donegá, A. Salant, U. Banin, G.D. Scholes, J.M. Lupton, A.L. Rogach, O. Benson, J. Feldmann, H. Weller, C. Spinella, R. Cingolani, T. Pellegrino, L. Manna, S.M. Park, T. Joo, S. Kim, L. Manna, A. Meijerink, D. Vanmaekelbergh, Synthesis and properties of colloidal heteronanocrystals, Chem. Soc. Rev. 40 (2011) 1512–1546, doi:10.1039/C0CS00055H.

[6] N.J. Borys, M.J. Walter, J. Huang, D.V. Talapin, J.M. Lupton, The role of particle morphology in interfacial energy transfer in CdSe/CdS heterostructure nanocrystals, Science 330 (2010) 1371–1374, doi:10.1126/science.1198070.

[7] M.A. Boles, D. Ling, T. Hyeon, D.V. Talapin, The surface science of nanocrystals, Nature Mater. 15 (2016) 141–153, doi:10.1038/nmat4526.

[8] Y. Yin, A.P. Alivisatos, Colloidal nanocrystal synthesis and the organic–inorganic interface, Nature 437 (2005) 664–670, doi:10.1038/nature04165.

[9] R. Ghosh Chaudhuri, S. Paria, Core/shell nanoparticles: classes, properties, synthesis mechanisms, characterization, and applications, Chem. Rev. 112 (2012) 2373–2433, doi:10.1021/cr100449n.

[10] S. Laurent, D. Forge, M. Port, A. Roch, C. Robic, L. Vander Elst, R.N. Muller, Magnetic iron oxide nanoparticles: Synthesis, stabilization, vectorization, physicochemical characterizations and biological applications, Chem. Rev. 108 (2008) 2064–2110, doi:10.1021/cr068445e.

[11] D. Knopp, D. Tang, R. Niessner, Review: Bioanalytical applications of biomolecule-functionalized nanometer-sized doped silica particles, Anal. Chim. Acta 647 (2009) 14–30, doi:10.1016/j.aca.2009.05.037.

[12] I.J. Kramer, E.H. Sargent, The architecture of colloidal quantum dot solar cells: Materials to devices, Chem. Rev. 114 (2014) 863–882, doi:10.1021/cr400299t.

[13] D.V. Talapin, J.-S. Lee, M.V. Kovalenko, E.V. Shevchenko, Prospects of colloidal nanocrystals for electronic and optoelectronic applications, Chem. Rev. 110 (2010) 389–458, doi:10.1021/cr900137k.

[14] M.V. Kovalenko, L. Manna, A. Cabot, Z. Hens, D.V. Talapin, C.R. Kagan, V.I. Klimov, A.L. Rogach, P. Reiss, D.J. Milliron, P. Guyot-Sionnnest, G. Konstantatos, W.J. Parak, T. Hyeon, B.A. Korgel, C.B. Murray, W. Heiss, Prospects of nanoscience with nanocrystals, ACS Nano (2015), doi:10.1021/nn506223h 150122081035000.

[15] C.R. Kagan, Flexible colloidal nanocrystal electronics, Chem. Soc. Rev. 48 (2019) 1626–1641, doi:10.1039/c8cs00629f.

[16] S. Tomić, N.M. Harrison, T.S. Jones, Electronic structure of QD arrays: application to intermediate-band solar cells, Opt. Quantum Electron. 40 (2008) 313–318, doi:10.1007/s11082-008-9228-3.

[17] L. Cuadra, A. Martí, A. Luque, Present status of intermediate band solar cell research, Thin Solid Films 451–452 (2004) 593–599, doi:10.1016/j.tsf.2003.11.047.

[18] Q. Shao, A.A. Balandin, A.I. Fedoseyev, M. Turowski, Intermediate-band solar cells based on quantum dot supracrystals, Appl. Phys. Lett. 91 (2007), doi:10.1063/1.2799172 163503.

[19] A. Luque, A. Martí, A.J. Nozik, Solar cells based on quantum dots: Multiple exciton generation and intermediate bands, MRS Bull. 32 (2007) 236–241, doi:10.1557/mrs2007.28.

[20] D.L. Nika, E.P. Pokatilov, Q. Shao, A.A. Balandin, Charge-carrier states and light absorption in ordered quantum dot superlattices, Phys. Rev. B 76 (2007) 1–9, doi:10.1103/PhysRevB.76.125417.

[21] Q. Zhang, W. Wei, Single intermediate-band solar cells of InGaN/InN quantum dot supracrystals, Appl. Phys. A. 113 (2013) 75–82, doi:10.1007/s00339-013-7826-9.

[22] A. Luque, A. Martí, C. Stanley, N. López, L. Cuadra, D. Zhou, J.L. Pearson, A. McKee, General equivalent circuit for intermediate band devices: Potentials, currents and electroluminescence, J. Appl. Phys. 96 (2004) 903–909, doi:10.1063/1.1760836.

[23] A. Martí, E. Antolín, C.R. Stanley, C.D. Farmer, N. López, P. Díaz, E. Cánovas, P.G. Linares, A. Luque, Production of photocurrent due to intermediate-to-conduction-band transitions: A demonstration of a key operating principle of the intermediate-band solar cell, Phys. Rev. Lett. 97 (2006), doi:10.1103/PhysRevLett.97.247701 247701.

[24] J. van Embden, J. Jasieniak, P. Mulvaney, J. van Embden, J. Jasieniak, P. Mulvaney, J. van Embden, J. Jasieniak, P. Mulvaney, Mapping the optical properties of cdse/cds heterostructure nanocrystals: The effects of core size and shell thickness, J. Am. Chem. Soc. 131 (2009) 14299–14309, doi:10.1021/ja9030209.

[25] J.J. Li, Y.A. Wang, W. Guo, J.C. Keay, T.D. Mishima, M.B. Johnson, X. Peng, Large-scale synthesis of nearly monodisperse CdSe/CdS core/shell nanocrystals using air-stable reagents via successive ion layer adsorption and reaction, J. Am. Chem. Soc. 125 (2003) 12567–12575, doi:10.1021/JA0363563.

[26] A. Dong, X. Ye, J. Chen, Y. Kang, T. Gordon, J.M. Kikkawa, C.B. Murray, A generalized ligand-exchange strategy enabling sequential surface functionalization of colloidal nanocrystals, J. Am. Chem. Soc. 133 (2011) 998–1006, doi:10.1021/ja108948z.

[27] J. Park, J. Joo, S.G. Kwon, Y. Jang, T. Hyeon, Synthesis of monodisperse spherical nanocrystals, Angew. Chem. Int. Ed. Engl. 46 (2007) 4630–4660, doi:10.1002/anie.200603148.

[28] M.J. Panzer, K.E. Aidala, V. Bulović, Contact printing of colloidal nanocrystal thin films for hybrid organic/quantum dot optoelectronic devices, Nano Rev. 3 (2012) 16144, doi:10.3402/nano.v3i0.16144.

[29] J. Jasieniak, B.I. MacDonald, S.E. Watkins, P. Mulvaney, Solution-processed sintered nanocrystal solar cells via layer-by-layer assembly, Nano Lett. 11 (2011) 2856–2864, doi:10.1021/nl201282v.

[30] A.W. Wills, M.S. Kang, A. Khare, W.L. Gladfelter, D.J. Norris, Thermally degradable ligands for nanocrystals, ACS Nano 4 (2010) 4523–4530, doi:10.1021/nn100637u.

[31] E.A. Slejko, V. Sayevich, B. Cai, N. Gaponik, V. Lughi, V. Lesnyak, A. Eychmüller, Precise engineering of nanocrystal shells via colloidal atomic layer deposition, Chem. Mater. 29 (2017) 8111–8118, doi:10.1021/acs.chemmater.7b01873.

[32] A.N. Goldstein, C.M. Echer, A.P. Alivisatos, Melting in semiconductor nanocrystals, Science 256 (1992) 1425–1427, doi:10.1126/science.256.5062.1425.

[33] W.D. Kingery, H.K. Bowen, D.R. Uhlmann, Introduction To Ceramics, second ed., John Wiley & Sons, Ltd, 1967 (Accessed 29 July 2019).

[34] C.N. Bucherl, K.R. Oleson, H.W. Hillhouse, Thin film solar cells from sintered nanocrystals, Curr. Opin. Chem. Eng. 2 (2013) 168–177, doi:10.1016/j.coche.2013.03.004.

[35] D.B. Mitzi, M. Yuan, W. Liu, A.J. Kellock, S.J. Chey, V. Deline, A.G. Schrott, A high-efficiency solution-deposited thin-film photovoltaic device, Adv. Mater. 20 (2008) 3657–3662, doi:10.1002/adma.200800555.

[36] M. Singh, K. Suganuma, Light energy induced sintering of Cu2ZnSnS4 nanocrystal-based film for solar cell, Nano-Struct. Nano-Objects 19 (2019), doi:10.1016/j.nanoso.2019.100369 100369.

[37] E.A. Slejko, V. Lughi, Size control at maximum yield and growth kinetics of colloidal II–VI semiconductor nanocrystals, J. Phys. Chem. C. 123 (2019) 1421–1428, doi:10.1021/acs.jpcc.8b07754.

[38] W.W. Yu, L. Qu, W. Guo, X. Peng, Experimental determination of the extinction coefficient of CdTe, CdSe, and CdS nanocrystals, Chem. Mater. 15 (2003) 2854–2860, doi:10.1021/cm034081k.

[39] J. Jasieniak, L. Smith, J. Van Embden, P. Mulvaney, M. Califano, Re-examination of the size dependent absorption properties of CdSe quantum dots, J. Phys. Chem. C. 113 (2009) 19468–19474.

[40] T.H. Tran, T.H. Pham, C.D. Sai, T.T. Nguyen, V.T. Nguyen, Study phase evolution of hydrothermally synthesized Cu 2 ZnSnS 4 nanocrystals by Raman spectroscopy, Nano-Struct. Nano-Objects 18 (2019), doi:10.1016/j.nanoso.2019.100273 100273.

[41] Z.A. Peng, X. Peng, Z. Adam Peng, X. Peng, Z.A. Peng, X. Peng, Formation of high-quality CdTe, CdSe, and CdS nanocrystals using CdO as precursor, J. Am. Chem. Soc. 123 (2001) 183–184, doi:10.1021/ja003633m.

[42] A.L. Efros, M. Rosen, M. Kuno, M. Nirmal, D.J. Norris, M. Bawendi, Band-edge exciton in quantum dots of semiconductors with a degenerate valence band: Dark and bright exciton states, Phys. Rev. B. 54 (1996) 4843–4856, doi:10.1103/PhysRevB.54.4843.

[43] L. De Trizio, L. Manna, Forging colloidal nanostructures via cation exchange reactions, Chem. Rev. 116 (2016) 10852–10887, doi:10.1021/acs.chemrev.5b00739.

[44] C. Bothe, A. Kornowski, H. Tornatzky, C. Schmidtke, H. Lange, J. Maultzsch, H. Weller, Solid-state chemistry on the nanoscale: Ion transport through interstitial sites or vacancies?, Angew. Chem., Int. Ed. Engl. 54 (2015) 14183–14186, doi:10.1002/anie.201507263.

[45] S.K. Mishra, R.K. Srivastava, S.G. Prakash, R.S. Yadav, A.C. Panday, Structural, photoconductivity and photoluminescence characterization of cadmium sulfide quantum dots prepared by a co-precipitation method, Electron. Mater. Lett. 7 (2011) 31–38, doi:10.1007/s13391-011-0305-6.

[46] K. Subba Ramaiah, R.D. Pilkington, A.E. Hill, R.D. Tomlinson, A.K. Bhatnagar, Structural and optical investigations on CdS thin films grown by chemical bath technique, Mater. Chem. Phys. 68 (2001) 22–30, doi:10.1016/S0254-0584(00)00281-9.

[47] V. Singh, P. Chauhan, Structural and optical characterization of CdS nanoparticles prepared by chemical precipitation method, J. Phys. Chem. Solids 70 (2009) 1074–1079, doi:10.1016/j.jpcs.2009.05.024.

[48] L. Brus, Electronic wave functions in semiconductor clusters: experiment and theory, J. Phys. Chem. 90 (1986) 2555–2560, doi:10.1021/j100403a003.

[49] J. Jasieniak, M. Califano, S.E. Watkins, Size-dependent valence and conduction band-edge energies of semiconductor nanocrystals, ACS Nano 5 (2011) 5888–5902, doi:10.1021/nn201681s.

[50] Y.E. Panfil, D. Shamalia, J. Cui, S. Koley, U. Banin, Electronic coupling in colloidal quantum dot molecules; the case of CdSe/CdS core/shell homodimers, J. Chem. Phys. 151 (2019), doi:10.1063/1.5128086 224501.

[51] S. Ithurria, D.V. Talapin, Colloidal atomic layer deposition (c-ALD) using self-limiting reactions at nanocrystal surface coupled to phase transfer between polar and nonpolar media, J. Am. Chem. Soc. 134 (2012) 18585–18590, doi:10.1021/ja308088d.
[52] M.V. Kovalenko, M.I. Bodnarchuk, J. Zaumseil, J.S. Lee, D.V. Talapin, Expanding the chemical versatility of colloidal nanocrystals capped with molecular metal chalcogenide ligands, J. Am. Chem. Soc. 132 (2010) 10085–10092, doi:10.1021/ja1024832.
[53] R. Ihly, J. Tolentino, Y. Liu, M. Gibbs, M. Law, The photothermal stability of PbS quantum dot solids, ACS Nano 5 (2011) 8175–8186, doi:10.1021/nn2033117.
[54] S.I. Sadovnikov, Thermal stability and recrystallization of semiconductor nanostructured sulfides and sulfide solid solutions, J. Alloys Compd. 788 (2019) 586–599, doi:10.1016/j.jallcom.2019.02.244.